Adaptive Fiber Source for Label-free Nonlinear Microscopy

by

Honghao Cao

B.S., Huazhong University of Science and Technology (2022)

Submitted to the Department of Electrical Engineering and Computer Science
in partial fulfillment of the requirements for the degree of

MASTER OF SCIENCE

at the

MASSACHUSETTS INSTITUTE OF TECHNOLOGY

May 2024

© 2024 Honghao Cao. All rights reserved.

The author hereby grants to MIT a nonexclusive, worldwide, irrevocable, royalty-free license to exercise any and all rights under copyright, including to reproduce, preserve, distribute and publicly display copies of the thesis, or release the thesis under an open-access license.

Authored by:	Honghao Cao Department of Electrical Engineering and Computer Science May 8, 2024
Certified by:	Sixian You Assistant Professor of Electrical Engineering and Computer Science Thesis Supervisor
Accepted by:	Leslie A. Kolodziejski Professor of Electrical Engineering and Computer Science Chair, Department Committee on Graduate Students

Adaptive Fiber Source for Label-free Nonlinear Microscopy

by

Honghao Cao

Submitted to the Department of Electrical Engineering and Computer Science
on May 8, 2024 in partial fulfillment of the requirements for the degree of

MASTER OF SCIENCE

ABSTRACT

Nonlinear microscopy enables label-free visualization of biological processes in live samples at sub-cellular spatial resolution and sub-millimeter penetration depth, enabling the *in-vivo* study of mechanisms underlying several cellular functions. Due to the low absorption cross-section of the two-photon and three-photon excitation processes, especially for the endogenous fluorophores, high peak power broadband laser sources are important in improving nonlinear microscopy generation efficiency. Multimode fibers (MMFs) are regaining interest as light sources due to their high-dimensional spatiotemporal nonlinear dynamics and scalability for high power. MMF sources with effective control of nonlinear processes would enable new possibilities in many areas, such as high-power fiber lasers, biomedical imaging, and chemical sensing, as well as a platform for investigation of intriguing physics phenomena. In this thesis, we present a simple yet effective way of controlling nonlinear effects at high peak power levels in MMFs. This is achieved by leveraging not only the spatial but also the temporal degrees of freedom during multimodal nonlinear pulse propagation using a programmable fiber shaper that introduces time-dependent disorders. We achieve high spectral-temporal-spatial tunability in the output laser pulses of the MMF, resulting in a broadband high-peak-power source. We further demonstrate its potential as a laser source for nonlinear microscopy through widely tunable two-photon and three-photon excitation. This approach provides possibilities for technological advances in a wide range of fields, such as nonlinear optics, biomedical imaging, and spectroscopy.

Thesis supervisor: Sixian You
Title: Assistant Professor of Electrical Engineering and Computer Science

Acknowledgments

I want to thank my family for their support throughout my academic journey.

I would like to express my sincere gratitude to my advisor, Prof. Sixian You. Her invaluable guidance and constructive suggestions have inspired my motivation in my research and helped me learn effective communication. I am grateful for the technical discussions and critical feedback she has dedicated to my research.

Furthermore, I wish to acknowledge the support of my fellow lab members, Kunzan Liu, Dr. Tong Qiu, Li-yu Yu, Kasey Shashaty, Jiashu Han, Dr. Kristina Monakhova, Ryan Mei, and Cassandra T. Ye, without whose contributions this thesis could not have been completed. Their willingness to share and collaborate has encouraged everyone in our lab to work together towards better research.

Contents

Title page **1**

Abstract **3**

Acknowledgments **5**

List of Figures **9**

List of Tables **13**

1 Introduction **15**

2 Supercontinuum Generation in Multimode Fibers **17**
- 2.1 Experimental Setup 17
- 2.2 Multimodal Nonlinear Pulse Propagation in SI MMF 18

3 Spectral-temporal-spatial Customization in Multimode Fibers **23**
- 3.1 Fiber Shaper Device Design and Optimization 23
- 3.2 Modulation of Multimodal Nonlinear Effects in SI MMF 25
- 3.3 Spectral-Temporal-Spatial Optimization of MMF Output 29

4 Enhanced Nonlinear Microscopy with Adaptive Multimode Fiber Source **33**
- 4.1 Derivation of the Multiphoton Generation Efficiency 33
- 4.2 Quantitative Analysis of the Enhancement 34
- 4.3 Point Spread Function Engineering 37
- 4.4 Label-free Nonlinear Microscopy on Tissues 39

5 Conclusion **43**

References **45**

List of Figures

2.1 **Schematic of the experimental setup.** The step-index multimode fiber is pumped by ultrafast laser pulses at a center wavelength of 1300 nm and a duration of 46 fs for supercontinuum generation. The output supercontinuum pulses are collimated by an off-axis parabolic mirror and directed to the characterization apparatus and imaging system. OPA: optical parametric amplifier; M: mirror; FM: flip-mirror; BPF: bandpass filter; BS: beam splitter; Spect: spectrometer; PMT: photomultiplier tube. 18

2.2 **Multimodal spectral broadening in SI MMF. a**, Spectral evolution as a function of increasing input pulse energy in a 30-cm-long SI MMF, showing the emergence of three spectral windows dominated by distinct nonlinear effects. **b**, Output spectra at selected input pulse energies. Top row presents the spectrally filtered near-field beam profiles at an input energy of 800 nJ, numbers above each profile denote the center wavelength and bandwidth of the bandpass filter applied. Numerical simulations are presented in dotted gray, with the seven modes assumed to be excited with equal energy and phase. For visualization purposes, the spectrum and beam profile at each input pulse energy is normalized to their respective peak values at that energy. 19

2.3 **Stability of the MMF source.** **a**, Spectral stability of the SI MMF source obtained from the output spectra recorded per second for a period of 1 hour. The solid black trace represents the mean value, and the surrounding gray region indicates the level of variation (quantified by the standard deviation) of the recorded spectra. **b**, Normalized output average power of the SI MMF source recorded per second for a period of 1 hour. A silicon-based photodiode sensor (Thorlabs PM16-130) was used to measure the optical power at wavelength below 1100 nm and a thermal power sensor (Thorlabs S425C-L) was used to measure the optical power of longer wavelengths and the whole band. The SI MMF was pumped by 800-nJ 46-fs pulses at 1300 nm. RSD: relative standard deviation. Source data are provided as a Source Data file. 21

3.1 **Fiber shaper device.** Two versions of the fiber shaper device are designed and fabricated through 3D printing (V1) and laser cutting (V2). The actuators are both based on stepepr motors. For V1, and V2, the motion transmission is done by gear-rack and lead screw, respectively. For V2, we added another unit for residual handling to further improve its reproducibility. All the results discussed in this thesis are based on fiber shaper device V1. The blue line represents the multimode fiber mounted on the device. 24

3.2 **Spectral tunability of the fiber shaper with different numbers of actuators.** **a–d**, The output spectra of the fiber-shaper-controlled SI MMF with 1 (**a**), 2 (**b**), 3 (**c**), and 5 (**d**) actuators, respectively. 25

3.3 **Spectral tunability of the fiber shaper with different displacement ranges.** **a–d**, The output spectra of the fiber-shaper-controlled MMF with a displacement range of 2.5 mm (**a**), 5 mm (**b**), 10 mm (**c**), and 20 mm (**d**), respectively, all with 5 actuators and a motion resolution of 5 mm. 26

3.4 **Spectral tunability of the fiber shaper with different actuator motion resolutions.** **a–d**, The output spectra of the fiber-shaper-controlled SI MMF with the actuator motion resolution set at 20 mm (**a**), 10 mm (**b**), 7 mm (**c**), and 5 mm (**d**), respectively, all with 5 actuators and a displacement range of 20 mm. 27

3.5 **Mechanisms of spatiotemporal control of nonlinear effects in SI MMFs using fiber shaper.** **a**, Photograph of the custom-designed fiber shaper at its initial state. **b**,**g**, Experimental results of 30-cm-long SI MMF (50/125 µm, 0.22 NA) (**b**) and GRIN MMF (50/125 µm, 0.2 NA) (**g**) with the same set of macro-bending applied. Representative spectra corresponding to three randomly chosen configurations out of a pool of 3125 configurations are highlighted in distinct colors. The input pulse energy of 500 nJ is experimentally limited by the laser-induced damage to the GRIN MMF. **c**,**h**, Normalized electrical field of the first six spatial modes in unperturbed SI MMF (**c**) and GRIN MMF (**h**), with the core-cladding interface marked in black. **d**,**i**, Illustrative examples of the refractive index profiles of straight (n_0) and curved (n) SI MMF (**d**) and GRIN MMF (**i**). n is approximately expressed by $n_0 + n_0 y/r_b$, where r_b represents the bend radius, which is set to 1 cm (the minimum value the fiber shaper can introduce by design). **e**,**j**, Linear mode coupling coefficient Q_{np} resulting from the macro-bending in **c**,**h** for the first six spatial modes in **b**,**g** in SI MMF (**e**) and GRIN MMF (**j**). **f**, Effective refractive index (n_{eff}) for the first six spatial modes in SI and GRIN MMFs. 28

3.6 **Performance of fiber shaper: optimization in spectral, temporal, and spatial domains.** **a**, Ultrabroadband spectral tunability, evaluated from a set of spectra acquired from 3125 states of the fiber shaper. **b**,**c**, Representative examples of modulations in spectral band energy (**b**) of selected single bands and dual-band (denoted by vertical dotted lines), showing the most enhanced (Enhancement) and suppressed (Suppression) cases; and in pulse duration and the associated spatial intensity profiles (**c**) for selected spectral bands, with the center wavelength and bandwidth denoted above each panel, and the FWHM of the autocorrelation signals annotated near each trace. . . 31

4.1 **Multiphoton microscopy with the fiber-shaper-controlled MMF source.** **a**–**h**, Demonstration of 2PF and 3PF imaging on fluorescent beads using OPA (**a**,**d**), initial fiber source (**b**,**e**,**g**), and optimized fiber source (**c**,**f**,**h**). The contrasts of the insets are adjusted for visibility. Scale bars: 20 µm. **i**–**q**, Characterization of the spectral (**i**,**l**,**o**), temporal (**j**,**m**,**p**), and spatial (**k**,**n**,**q**) properties of the output beam of the initial and optimized fiber source corresponding to the images in **a**–**h**. The 50-nm spectral band energy and the FWHM of the autocorrelation (AC) signals are indicated in the figures. The spatial profiles are individually normalized to their maximum intensity. . . . 35

4.2 **PSF measurement of the 3PF excitation with the laser (reference) and the 2PF and 3PF excitation with the fiber source.** The size of the bead is 0.1 µm. 37

4.3 **Qualitative PSF comparison of the 2PF excitation (900 nm) and the 3PF excitation (1300 nm) with the fiber source under random bending conditions induced by the fiber shaper's different states.**The size of the bead is 1 µm. 38

4.4 **Normalized output spatial profiles of a 10-µm core step-index multimode fiber under various bending conditions.** **a**, Initial near-field intensity profile of the fiber output, showing a mixture of approximately three spatial linearly polarized (LP) modes. **b-g**, Near-field intensity profiles of the fiber output under various bending conditions, showing different combinations of the LP_{01} and the LP_{11} with two-fold spatial degeneracy. Each profile is individually normalized. 39

4.5 **Schematic of the multiphoton imaging setup.** PM: parabolic mirror; BPF: bandpass filter; DM: dichroic mirror; LP: long pass; OBJ: objective lens; PMT: photomultiplier tube. 40

4.6 **Nonlinear Microscopy with Adaptive Fiber source** Mouse whisker pad tissue imaging at 1225 nm excitation using the initial and optimized fiber source, showing THG signals of adipocytes, 3PAF signals of muscles, and SHG signals of collagen fibers. The contrasts of the insets are adjusted for visibility. Scale bars: 200 µm. 41

List of Tables

4.1 Multiphoton generation signal intensity enhancement 36

Chapter 1

Introduction

Multimode fibers (MMFs) have emerged as compelling light sources for nonlinear multiphoton microscopy (MPM) due to their high power scalability and versatile degrees of freedom for guided waves [1]–[7]. The complex intermodal interactions and nonlinear effects produce a supercontinuum spectrum ranging from the visible to the near-infrared domain. High spectral diversity across a broadband spectrum is critical for MPM as different fluorophores require different excitation wavelengths, and the multiphoton excitation processes require high peak power.

The use of MMFs in MPM, however, brings new challenges. Complex mode coupling and dispersion that create speckles and temporal broadening [8] bring complex output beam characteristics. These effects spread the pulse energy across the temporal, spatial, and spectral domains, thus reducing the peak power and efficiency of multiphoton signal generation. Controlling the spatiotemporal dynamics of nonlinear pulse propagation in MMFs is an important direction to overcome such limitations.

Over the past decades, significant progress has been made in studying and controlling nonlinear effects in MMFs. More importantly, the complex spatiotemporal dynamics and intermodal interactions in MMFs provide a platform for controlling nonlinear wave propagation, opening up possibilities for novel physics and new applications such as spatiotemporal light control [9]–[11], optical wave turbulence [8], [12], [13], and nonlinear frequency generation [14]–[17].

Recent developments in wavefront shaping techniques have enabled control of light propagation in complex media, including MMFs [18]–[23]. These studies have shown potential for tunable high-peak-power MMF light sources. However, existing studies have primarily focused on the spatial control of pulse propagation in graded-index (GRIN) MMFs [18]–[23], which fundamentally limits the tunablity in many applications due to two major problems: difficulty in control and limited broadband spectral brilliance.

MMF sources with more tunability and broadband spectral brilliance will bring new opportunities to biomedical imaging. To realize this potential, harnessing the untapped potential of temporal degrees of freedom to control nonlinear effects in MMFs at high peak power levels presents a compelling solution.

An innovative approach for the control of nonlinear pulse propagation in MMFs by utilizing both spatial and temporal degrees of freedom is proposed in this thesis. In this proposed method, accurate mechanical perturbations on different axial positions along the MMF are implemented to modulate the refractive index profile to induce targeted mode coupling. The perturbations are optimized by using adaptive algorithms to manipulate the spectral, temporal, and spatial properties of the output beam to improve the efficiency of multiphoton signal generation.

Precisely controlled pressing, (i.e. fiber pianos) were recently proposed to modulate the linear regime of temporal light propagation in the MMFs [24]–[27], which demonstrated more effective control due to the addition of the temporal domain (i.e. the additional two dimensions in a transmission matrix compared to the input wavefront). Although it is challenging to directly adopt the proposed fiber pianos to the nonlinear regime due to practical issues such as light loss and reproducibility, the idea of bringing such temporal control into the nonlinear regime is intriguing because of the high dimensionality of nonlinear pulse propagation.

The remainder of this thesis is outlined below. Chapter 2 introduces the experimental setup and supercontinuum generation results of the step-index (SI) MMF that is used throughout this work. Chapter 3 discusses the spectral-temporal-spatial customization of the multimode fiber by a programmable fiber shaper device. Chapter 4 focuses on the demonstration of the adaptive multimode fiber source application in nonlinear microscopy. Chapter 5 is a conclusion of this thesis and discusses limitations and potential future work.

Chapter 2

Supercontinuum Generation in Multimode Fibers

2.1 Experimental Setup

Ultrafast laser pulses at a center wavelength of 1300 nm and a duration of 46 fs (Light Conversion Cronus-3P) were pumped into a 30-cm-long SI MMF (50/125 µm, 0.22 NA). The beam was weakly focused into the fiber to induce a wide array of nonlinear optical effects, including self-phase modulation (SPM), cross-phase modulation (XPM), four-wave mixing (FWM), multimode soliton formation, and dispersive wave emission. The fiber was mounted on a 3D-printed programmable fiber shaper device that introduces multi-point macro-bending to the MMF through five individually controlled motorized actuators (Fig. 2.1). Each actuator acts as a bending unit that locally and precisely applies curvature on the fiber at different positions, producing local index perturbation and thus causing mode coupling [28], [29] at multiple time points of the pulse evolution. This setup gives a high-dimensional spatiotemporal control of the multimode nonlinear pulse propagation, thus making it possible for simultaneous control of spectral, spatial, and temporal profiles of the fiber output pulses. Besides the ease of construction and operation, the fiber shaper maintains high light throughput with not working bandwidth limitation and negligible light loss regardless of the actuator configurations, measured at ±1% at high power levels (800 nJ, 85% coupling efficiency at initial states).

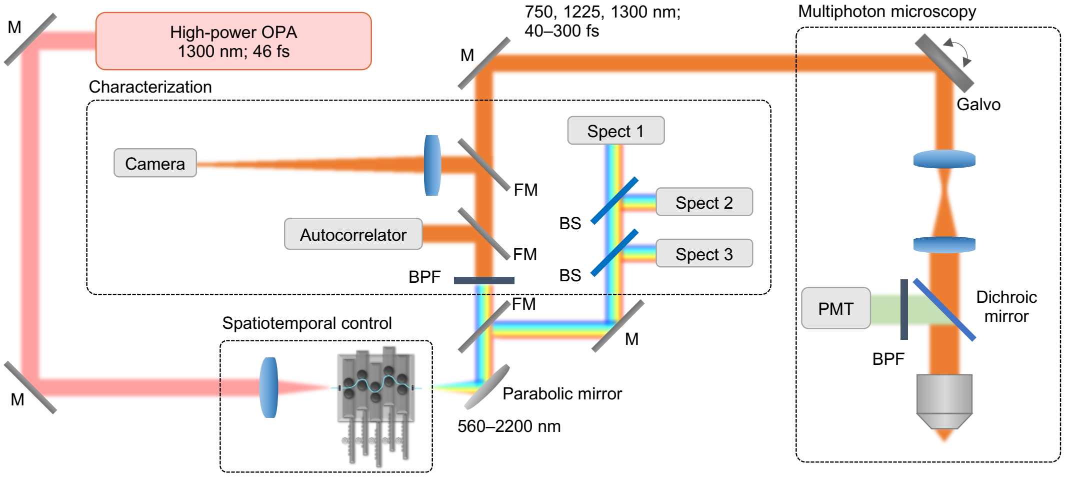
M
High-power OPA
1300 nm; 46 fs
750, 1225, 1300 nm;
40–300 fs
Multiphoton microscopy
M
Characterization
Galvo
Spect 1
Camera
FM
Spect 2
BS
Autocorrelator
FM
Spect 3
BS
BPF
FM
PMT
Dichroic mirror
Spatiotemporal control
M
BPF
M
Parabolic mirror
560–2200 nm

Figure 2.1: **Schematic of the experimental setup.** The step-index multimode fiber is pumped by ultrafast laser pulses at a center wavelength of 1300 nm and a duration of 46 fs for supercontinuum generation. The output supercontinuum pulses are collimated by an off-axis parabolic mirror and directed to the characterization apparatus and imaging system. OPA: optical parametric amplifier; M: mirror; FM: flip-mirror; BPF: bandpass filter; BS: beam splitter; Spect: spectrometer; PMT: photomultiplier tube.

2.2 Multimodal Nonlinear Pulse Propagation in SI MMF

We first investigated the evolution of the MMF output spectra with gradually increasing input pulse energy by using the characterization setup as depicted in Fig. 2.1 to understand the broadening behavior and the tuning mechanisms. The fiber shaper was set to its initial state with no bending applied to the fiber. The results are presented in Fig. 2.2a. As the injected pulse energy gradually increases, SPM, XPM, and intermodal FWM begin to dominate the spectral broadening process. As the input energy increases further, the output spectrum extends to the anomalous dispersion regime and multimode solitons (i.e., solitary waves consisting of multiple spatial modes) begin to form, due to the balancing between the nonlinear phase modulation and dispersive effects including the intramodal group velocity dispersion and intermodal velocity mismatch [30]. Meanwhile, excess energy from the soliton fission process is emitted as dispersive waves through the interaction between the nonlinear and higher-order dispersion effects. The dispersive waves are generated at shorter wavelengths to satisfy the phase-matching condition [31].

With further increase in input energy, the multimode soliton undergoes a redshift, resembling soliton self-frequency shifting [2], and eventually the spectrum extends beyond the near-infrared-II region. Accordingly, the phase-matched dispersive waves shift towards the

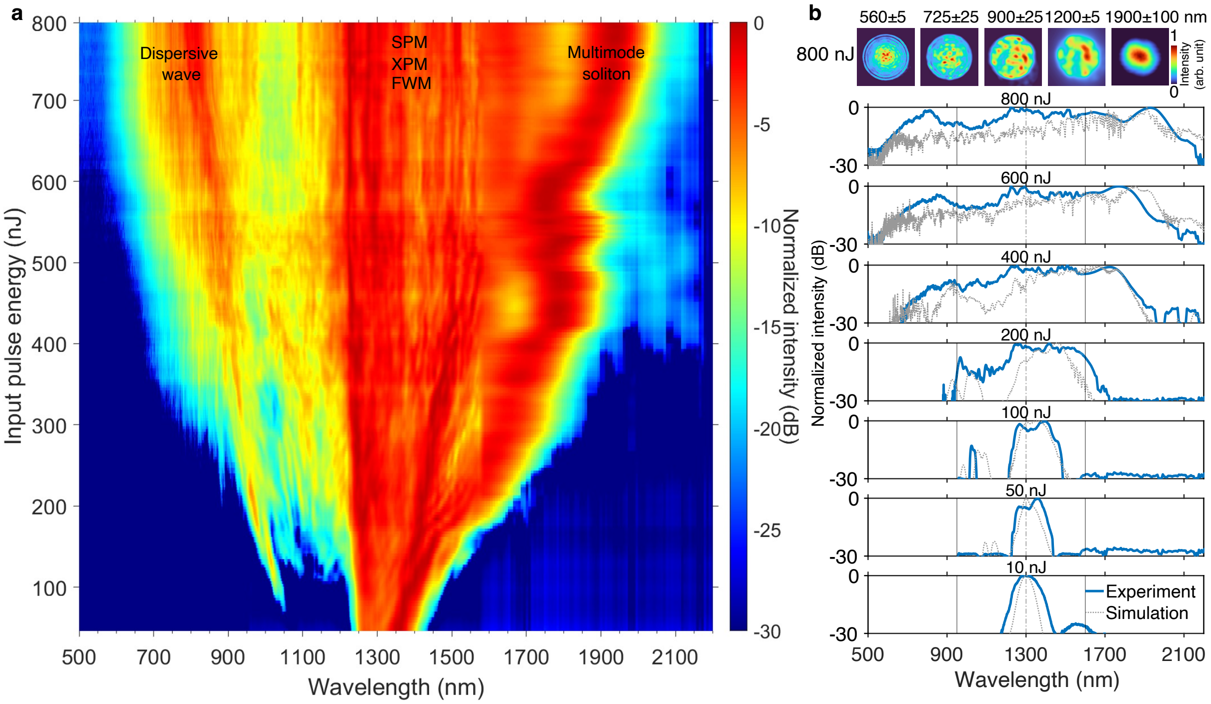

Figure 2.2: **Multimodal spectral broadening in SI MMF. a**, Spectral evolution as a function of increasing input pulse energy in a 30-cm-long SI MMF, showing the emergence of three spectral windows dominated by distinct nonlinear effects. **b**, Output spectra at selected input pulse energies. Top row presents the spectrally filtered near-field beam profiles at an input energy of 800 nJ, numbers above each profile denote the center wavelength and bandwidth of the bandpass filter applied. Numerical simulations are presented in dotted gray, with the seven modes assumed to be excited with equal energy and phase. For visualization purposes, the spectrum and beam profile at each input pulse energy is normalized to their respective peak values at that energy.

visible region. These observations are in agreement with the findings reported in [31], [32] with input wavelengths deeper into the anomalous dispersion regime. In addition, the fiber output power at 800-nJ input pulse energy was monitored for 1 hour to assess its stability (Fig. 2.3), which was measured to reflect 1–2% fluctuations at different wavelengths. Despite exceeding the critical power for catastrophic self-focusing (about 8 MW for silica at 1300 nm [33]), the pronounced dispersion effects associated with ultrashort pulses can effectively modify the dynamics of self-focusing, thereby preventing the exponential increase in peak intensity [34]. In this study, the fiber source was stable enough to generate reproducible output modulation and biological images. Nevertheless, the fluctuation metric could potentially be improved by using a better power meter (low dynamic range was used for the wavelength range above 1100 nm in this study), a more environmentally controlled optical space (temperature and humidity), and a more isolated fiber configuration (gel or air isolation).

To validate our experimental results, we performed numerical simulations (Fig. 2.2b) using the simplified (1+1)D model based on the generalized multimode nonlinear Schrödinger equation (GMMNLSE) [35], [36] with the same fiber parameters and launching conditions as in the experiments. Only the first seven radially symmetric modes are included to save computation time. Overall, we observed a good agreement in the spectral broadening between the experimental and numerical results at all energy levels. The discrepancy in distribution of spectral intensity is likely due to the limited number of modes in the simulation, which may not fully capture the multimodal nonlinear broadening in experiments.

To understand the multimodal compositions of the spatiotemporal nonlinear effects in SI MMF, the fiber output was spatially profiled with multiple spectral bands of interest (top row in Fig. 2.2b). The wavelength-dependent spatial profiles of the fiber output indicate that the lower-order modes are responsible for the formation of the most red-shifted multimode soliton (1900±100 nm; Fig. 2.2b), whereas the generation of the dispersive waves (560±5 nm, 725±25 nm; Fig. 2.2b) is dominated by the higher-order radially symmetric modes, as predicted in [31], to satisfy the intermodal phase-matching condition between one of the modes comprising the dispersive waves and another lower-order mode of the multimode soliton. The region in between (i.e., SPM, XPM, and FWM) (900±25 nm, 1200±5 nm; Fig, 2.2b) exhibits a high degree of multimodal behavior, which could be attributed to the many degrees of freedom required to satisfy the intermodal group velocity matching and intermodal phase matching [17], [37], [38]. These mechanistic studies and observations not only shed light on the underlying mechanisms of the two-octave spectral broadening, but also highlight the multimodal compositions of the spectral broadening in different dispersion regimes, which lays the foundation for the broadband tunability discussed in the following sections.

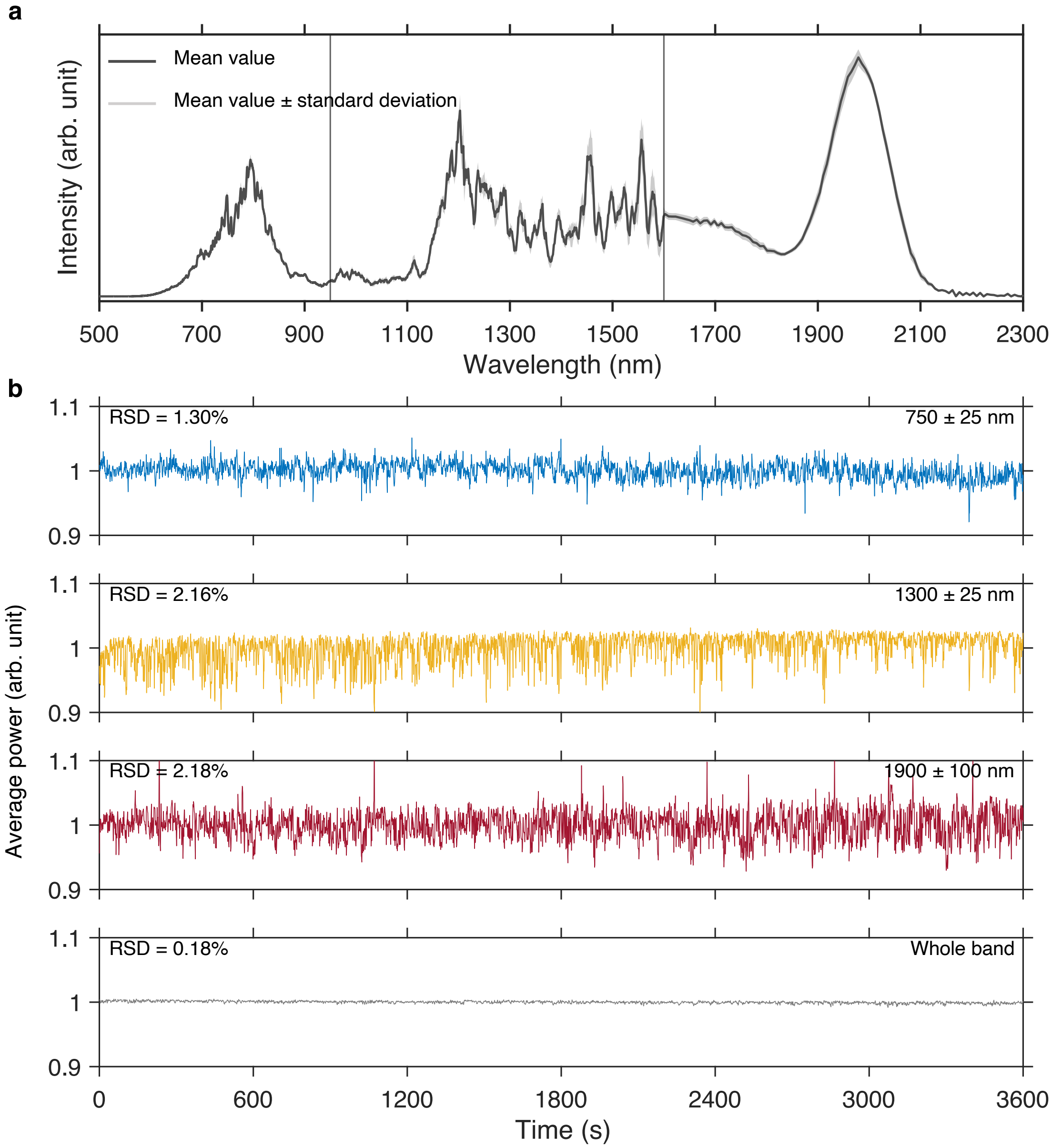

Figure 2.3: **Stability of the MMF source.** **a**, Spectral stability of the SI MMF source obtained from the output spectra recorded per second for a period of 1 hour. The solid black trace represents the mean value, and the surrounding gray region indicates the level of variation (quantified by the standard deviation) of the recorded spectra. **b**, Normalized output average power of the SI MMF source recorded per second for a period of 1 hour. A silicon-based photodiode sensor (Thorlabs PM16-130) was used to measure the optical power at wavelength below 1100 nm and a thermal power sensor (Thorlabs S425C-L) was used to measure the optical power of longer wavelengths and the whole band. The SI MMF was pumped by 800-nJ 46-fs pulses at 1300 nm. RSD: relative standard deviation. Source data are provided as a Source Data file.

Chapter 3

Spectral-temporal-spatial Customization in Multimode Fibers

3.1 Fiber Shaper Device Design and Optimization

To generate precisely controlled marco-bending to the fiber, we designed a device called fiber shaper. Two versions (V1 and V2, as shown in Fig. 3.1) have been designed and fabricated by 3D printing and laser cutting, respectively. The version used in this thesis is V1, and all the experimental results discussed in this thesis are based on V1. The V1 device was fabricated using 3D printing (Stratasys Fortus 380mc) with acrylonitrile styrene acrylate material. The fiber shaper features a rectangular base with five slots that can hold the translating units and constrain their linear motion in the desired direction. Each translating unit is powered by its own stepper motor (ELEGOO 28BYJ-48) through a 3D-printed rack and pinion system, allowing for individual control over their linear motion through a microcontroller (ELEGOO Mega R3) that communicates with a computer. To mount the fiber onto each translating unit, it is passed through a 0.5-mm-wide gap created by two disks and secured in place with a square cap. This design minimizes tension on the fiber during bending, and two half-disks with securing caps at the entrance and exit of the device ensure optimal functionality.

The radius of the disk, which determines the minimum bend radius the fiber shaper can apply, is designed to be 10 mm to minimize bending-induced transmission loss. Different device parameters were tested to optimize the spectral tunability of the fiber shaper. As a result, the rich combinations of actuator translation displacements create a vast array of fiber shape configurations, allowing for effective utilization of the spatial and temporal degrees of freedom in controlling nonlinear pulse propagation in SI MMFs with high light throughput.

The fiber shaper enables spatiotemporal control of the nonlinear effects in SI MMFs,

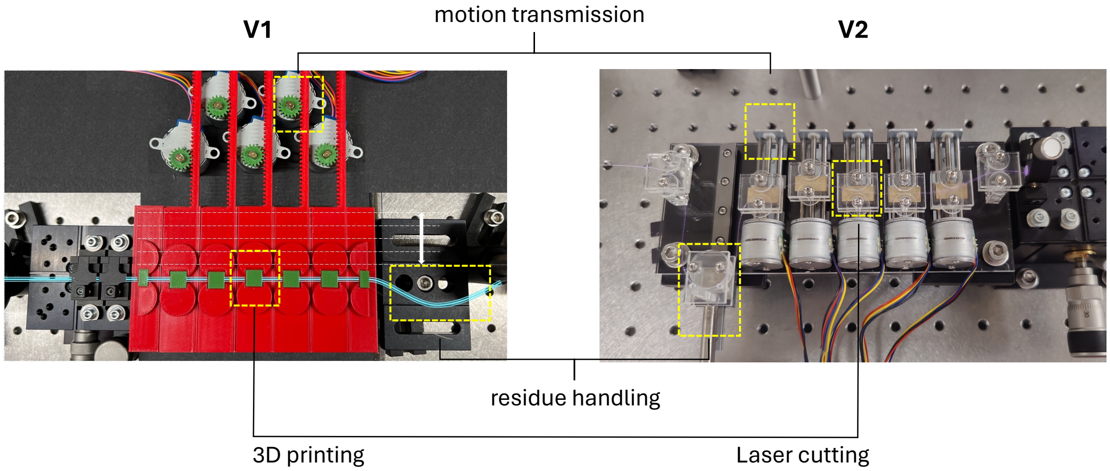

Figure 3.1: **Fiber shaper device.** Two versions of the fiber shaper device are designed and fabricated through 3D printing (V1) and laser cutting (V2). The actuators are both based on stepepr motors. For V1, and V2, the motion transmission is done by gear-rack and lead screw, respectively. For V2, we added another unit for residual handling to further improve its reproducibility. All the results discussed in this thesis are based on fiber shaper device V1. The blue line represents the multimode fiber mounted on the device.

underlying great tunability in the fiber source properties to adapt to diverse applications. To maximize this tunability, we investigate several key parameters involved in the design of the fiber shaper. These parameters include the number of actuators, as well as the total range and resolution of the actuator's linear motion. The impact of these parameters on the 900–1700 nm band are shown in Figs. 3.2–3.4, where we define an average spectral tuning ratio (η) to quantify the tunability:

$$\eta = \frac{1}{N} \sum_{n=1}^{N} \frac{I_{\lambda_n}^{\max}}{I_{\lambda_n}^{\min}}. \tag{3.1}$$

N denotes the number of discrete wavelengths acquired by the spectrometers, $I_{\lambda_n}^{\max}$ and $I_{\lambda_n}^{\min}$ refer to the maximum and minimum intensity at each wavelength. Our results indicate that the performance is optimized when using 5 actuators, a displacement range of 20 mm, and an actuator motion resolution of 5 mm. Notably, these parameters are specifically tailored to this device and may require adjustments for devices with different physical dimensions.

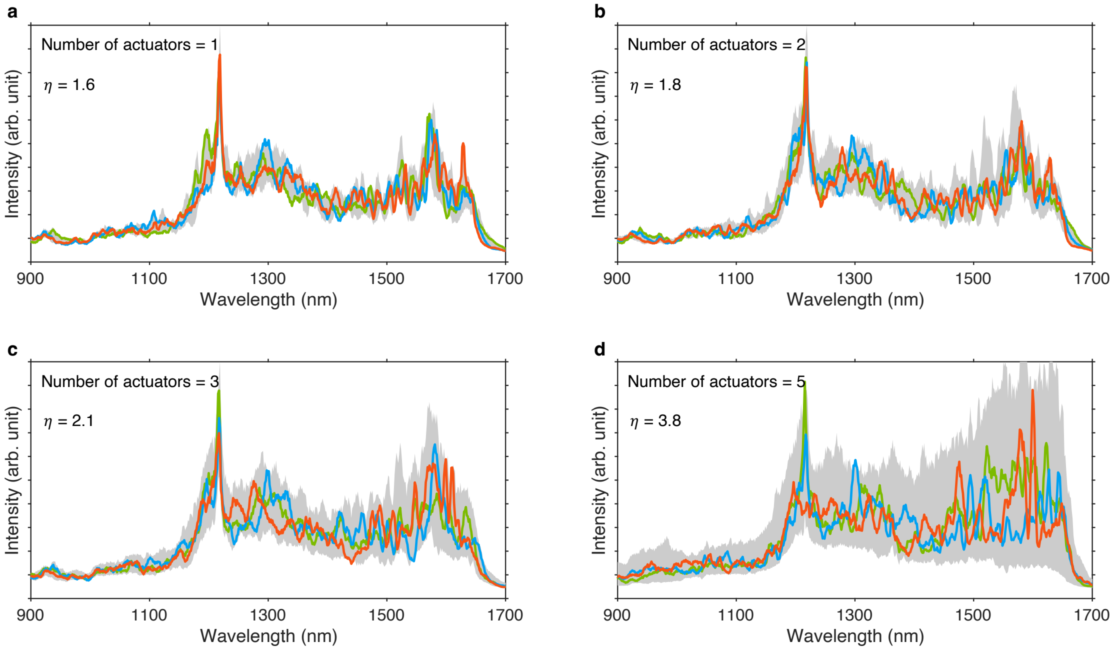

Figure 3.2: **Spectral tunability of the fiber shaper with different numbers of actuators. a–d**, The output spectra of the fiber-shaper-controlled SI MMF with 1 (**a**), 2 (**b**), 3 (**c**), and 5 (**d**) actuators, respectively.

3.2 Modulation of Multimodal Nonlinear Effects in SI MMF

By controlling the relative shift between the actuators, macro-bending of various radii can be applied to the fiber precisely and simultaneously, allowing for an exhaustive automated search and adaptive optimization of thousands of fiber shape configurations to achieve optimal output spectrotemporal properties. This can be readily scaled up with more actuators to unlock the full high-dimensional spatiotemporal control of the multimodal nonlinear optics. In principle, these actuators alter the local refractive index profile, causing energy coupling between modes at multiple time points during the pulse evolution, which altogether enable the high-dimensional spatiotemporal control of the multimode nonlinear pulse propagation. This process can be modeled by supplementing the GMMNLSE on the right-hand side with an additional term representing the linear mode coupling effect [36], [37], [39]:

$$i\sum_{n}^{N} Q_{np} A_n e^{i(\beta_n-\beta_p)z}, \tag{3.2}$$

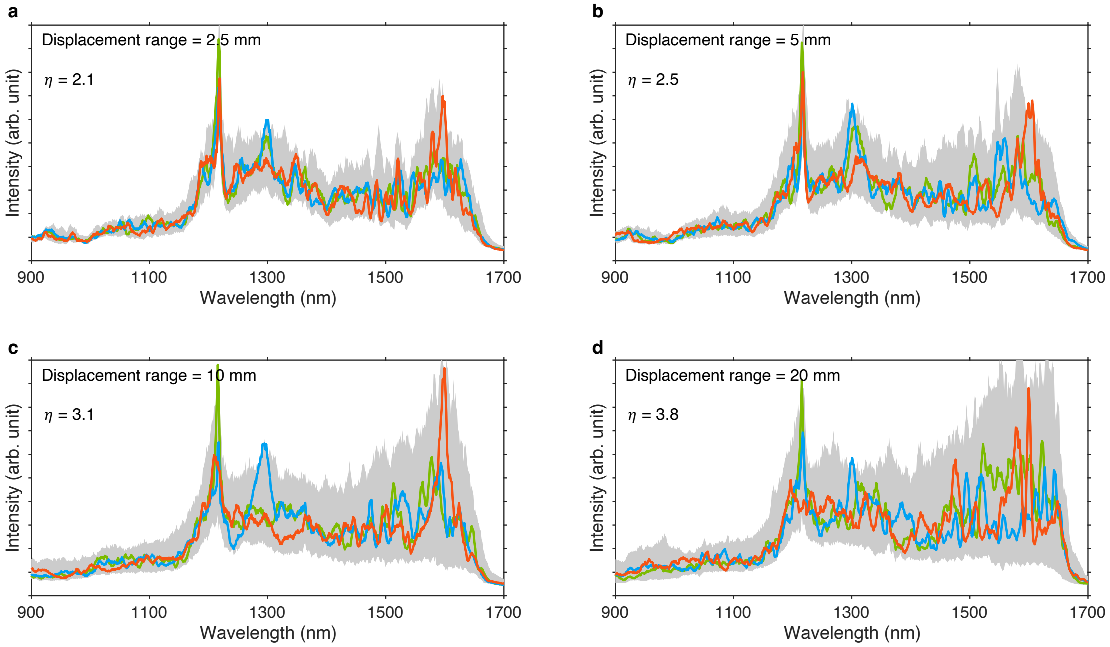

Figure 3.3: **Spectral tunability of the fiber shaper with different displacement ranges. a–d**, The output spectra of the fiber-shaper-controlled MMF with a displacement range of 2.5 mm (**a**), 5 mm (**b**), 10 mm (**c**), and 20 mm (**d**), respectively, all with 5 actuators and a motion resolution of 5 mm.

where Q_{np} denotes the linear coupling coefficient between mode-n and mode-p due to a local perturbation, determined by the spatial overlap of the three quantities. An additional exponential term, in comparison to [36], is included to account for the effects of phase mismatch. The modes can be simplified as the ideal modes of the unperturbed waveguide using perturbative coupled-mode theory in principle [40]. However, in practice, the mode field can undergo considerable deformation in curved multimode fibers, making it necessary to consider additional variations related to mode field deformation, such as changes in the propagation constant and the nonlinear coupling coefficient S^K_{plmn} and S^R_{plmn}, which is determined by the spatial overlap between the mode-p, -l, -m, and -n. As a result, by introducing localized changes to Q_{np} and the mode fields at axially dispersed positions along the fiber, the spatial and temporal degrees of freedom of nonlinear pulse propagation can be simultaneously controlled.

The perturbed GMMNLSE and the observed evolution of the spectral broadening and spatial profiles provide a key insight into the condition of effective spatiotemporal control of multimodal nonlinear optical processes in multimode fibers. At individual temporal instances, the more effectively we can modulate the linear and nonlinear mode coupling coefficients and the mode propagation constant, the higher-dimensional control and the greater

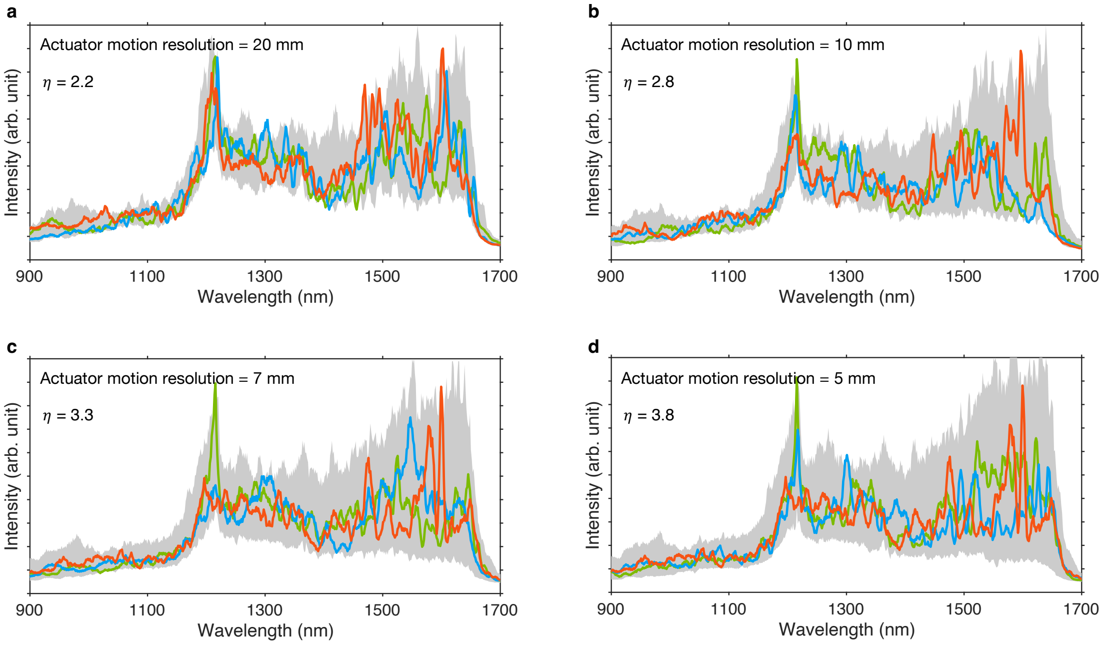

Figure 3.4: **Spectral tunability of the fiber shaper with different actuator motion resolutions. a–d**, The output spectra of the fiber-shaper-controlled SI MMF with the actuator motion resolution set at 20 mm (**a**), 10 mm (**b**), 7 mm (**c**), and 5 mm (**d**), respectively, all with 5 actuators and a displacement range of 20 mm.

tunability the source will exhibit. Almost all previous multimodal nonlinear pulse propagation studies focused on GRIN MMFs due to their unique self-imaging properties and low modal dispersion. However, we observed that SI MMFs exhibit significantly greater tunability and higher spectral brilliance under the same experimental conditions (Fig. 3.5). This is likely due to their larger modal areas and the more closely spaced propagation constants, which collectively lead to lower peak intensity, higher sensitivity to bending, and increased susceptibility to the mode coupling effect.

To gain a mechanistic understanding of this phenomenon, we simulated the effect of bending for the two fiber types using the perturbative coupled-mode theory for simplicity, which assumes that the mode fields are not deformed by the weak perturbation. Figure 3.5 displays the simulation results for the SI and GRIN MMFs, showcasing the linear interactions between the first six spatial modes in curved fibers as an illustrative example. The resulting linear coupling coefficient is presented in Fig. 3.5e,j. The phase mismatch is reflected by the effective refractive index n_{eff} in Fig. 3.5f. We chose 1 cm as the bend radius in simulation since it is the minimum value the fiber shaper can introduce by design. The simulation results show that SI MMF has a greater Q_{np} and smaller phase mismatch, both of which contribute positively to the strength of linear coupling reflected by equation (3.2), indicating

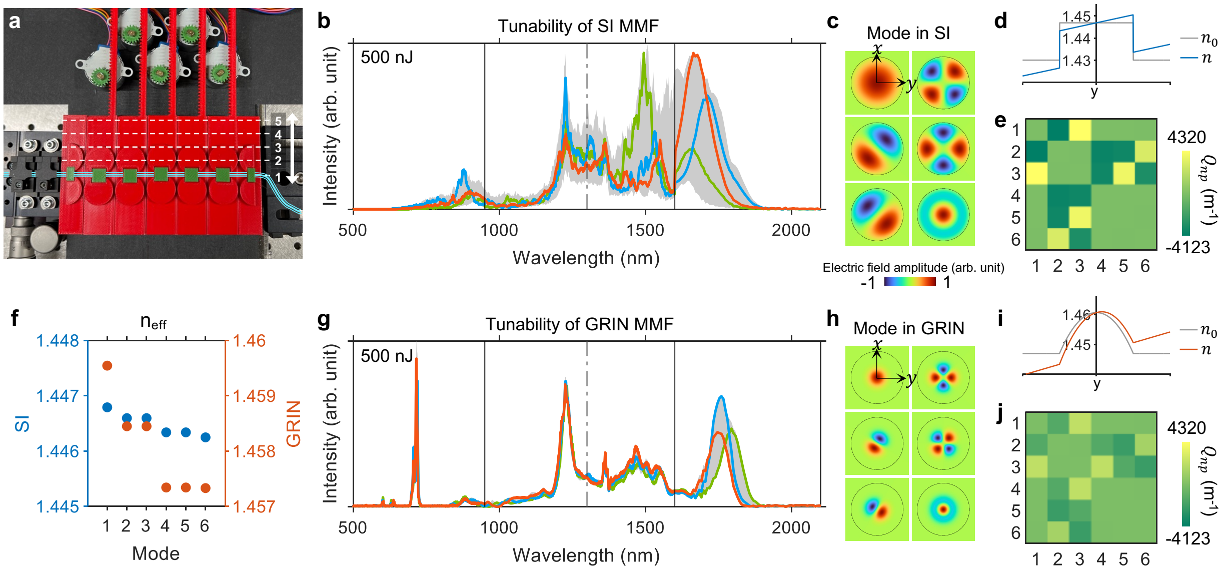

Figure 3.5: **Mechanisms of spatiotemporal control of nonlinear effects in SI MMFs using fiber shaper.** **a**, Photograph of the custom-designed fiber shaper at its initial state. **b**,**g**, Experimental results of 30-cm-long SI MMF (50/125 µm, 0.22 NA) (**b**) and GRIN MMF (50/125 µm, 0.2 NA) (**g**) with the same set of macro-bending applied. Representative spectra corresponding to three randomly chosen configurations out of a pool of 3125 configurations are highlighted in distinct colors. The input pulse energy of 500 nJ is experimentally limited by the laser-induced damage to the GRIN MMF. **c**,**h**, Normalized electrical field of the first six spatial modes in unperturbed SI MMF (**c**) and GRIN MMF (**h**), with the core-cladding interface marked in black. **d**,**i**, Illustrative examples of the refractive index profiles of straight (n_0) and curved (n) SI MMF (**d**) and GRIN MMF (**i**). n is approximately expressed by $n_0 + n_0 y/r_b$, where r_b represents the bend radius, which is set to 1 cm (the minimum value the fiber shaper can introduce by design). **e**,**j**, Linear mode coupling coefficient Q_{np} resulting from the macro-bending in **c**,**h** for the first six spatial modes in **b**,**g** in SI MMF (**e**) and GRIN MMF (**j**). **f**, Effective refractive index (n_{eff}) for the first six spatial modes in SI and GRIN MMFs.

that richer spatiotemporal dynamics can be introduced in SI MMFs with the application of macro-bending. The significantly smaller Q_{np} exhibited by GRIN MMFs can be attributed to the more confined mode field which sees weaker local perturbation at the center region and hence higher resistance to mechanical deformation such as bending [41]–[43]. Moreover, the clustering nature of the propagation constants in GRIN MMFs makes the perturbation-induced mode coupling tend to occur between the nearly degenerate modes, that is, the so-called degenerate-mode group [44]. Both factors make the multimodal nonlinear dynamics in GRIN MMFs less sensitive to fiber bending compared to that in SI MMFs.

Apart from the tunability, we also observed that the GRIN MMFs exhibit a lower threshold for laser-induced damage. As we gradually increased the input pulse energy, we noticed fiber damage along with a decrease in total output power and a reduction in the output spectral span. This lower damage threshold is possibly due to the parabolic index profile which leads to more severe self-focusing effects [5], and the Germanium dopant in the GRIN fiber core [45]. These analyses and observations provide insights into the mechanism of fiber-shaper-based spatiotemporal control and validate the choice of SI MMFs for a two-octave, high-peak-power, tunable fiber source. Our observation, although unexpected, is consistent with the recent studies that show GRIN MMFs are not as sensitive to launching conditions or bending as SI MMFs [32], [42], [43]. Despite it being a drawback to applications that demand insensitivity to bending, the usually undesirable susceptibility to bending of SI MMFs, together with their power scalability, are essential for achieving effective spatiotemporal control of high-power pulse propagation in multimode fibers.

3.3 Spectral-Temporal-Spatial Optimization of MMF Output

We next evaluate the effectiveness of using fiber shaper to control nonlinear effects in SI MMFs by examining the tunability in spectral band energy (Fig. 3.6a,b), temporal duration (Fig. 3.6c), and spatial intensity profiles (Fig. 3.6c) of the output light field while shaping the fiber in real-time.

Figure 3.6a shows the spectral tunability factor across a continuous two-octave bandwidth, by exhausting the combination of actuator positions on the fiber shaper. The spectral tunability factor is defined as the ratio of the maximally enhanced intensity to the maximally suppressed intensity for each 20-nm-wide spectral band. We observed that the tunability varies substantially across the spectrum, with the minimum enhancement ratio of 3.1-fold shown in the middle of the spectral span, and significantly higher enhancement ratios ranging from 9-fold to as much as 166-fold at the two ends of the spectrum (below 800 nm and above 1500 nm). Such wavelength dependence is very likely to be the product of distinct broadening mechanisms in different dispersion regimes. To look into the versatility and effectiveness of the fiber shaper in manipulating various nonlinear effects, we next show in Fig. 3.6b,c representative examples in different spectral regions, each featuring distinct dominant broadening mechanisms. The highest spectral tunability lies in the dispersive wave regime (500–900 nm; Fig. 3.6b) and the soliton regime (1700–2300 nm; Fig. 3.6b), the 9-fold and 166-fold marked in Fig. 3.6a are shown as instances in Fig. 3.6b. Simultaneous dual-band spectral tuning, with an averaged enhancement ratio of 2.3-fold for the two bands, is exemplified for the nonlinear phase modulation regime (1000–1600 nm; Fig. 3.6b).

Multimode solitons and their phase-matched dispersive waves consist of multiple mode combinations, within each combination the modes are group-velocity matched [30]. Mechanical perturbations such as a series of macro-bending can cause major changes in the few-mode composition and thus significantly alter spectral profiles in order to re-match the group velocity via mode-dependent spectral shifting. This is also manifested by dramatic changes of the few-mode-like spatial intensity profiles of multimode solitons (1700±42.5 nm and 1900±100 nm; Fig. 3.6c) and dispersive waves (750±25 nm; Fig. 3.6c) across seven random states of the fiber shaper. These changes reflect the capability of the fiber shaper to significantly alter the mode composition, and thus the output light field in the spectral and spatial domains. The temporal duration at the fiber output, on the other hand, shows limited tunability as solitons and dispersive waves are intrinsically nearly transform-limited pulses. In contrast, the regime dominated by SPM, XPM, and FWM are known for highly nonlinear, strongly coupled, and highly multimodal behavior. The resulting spectrum is the incoherent summation of many modes, which makes spectral shape less sensitive to modal distribution changes and reduces the effectiveness of tuning the spectral intensity. The speckled spatial intensity profile (1300±25; Fig. 3.6c) corroborates the highly multimode nature of the nonlinear phase modulation process, in which the many-mode composition is needed to satisfy the intermodal phase-matching and velocity-matching conditions. Interestingly, the control in the temporal domain is much more significant in the nonlinear phase modulation regime than other regimes, ranging from 1523 to 352 fs based on the full-width at half-maximum (FWHM) of the autocorrelation signals, from 1080 to 250 fs assuming a Gaussian pulse shape for simplicity. This observation can be attributed to the effective reduction of modal dispersion in the multimodal output through optimization of fiber shaper-induced linear mode coupling.

Our results demonstrate that the fiber shaper effectively manipulates the modal compositions of the propagating pulse and the resulting spectro-spatio-temporal properties of the output light field, exceeding what can be achieved through spatial control of the fiber input. The intricate nonlinear interactions emphasize the benefits of using a fiber shaper to control the spatiotemporal dimension of the nonlinear dynamics in order to achieve a targeted output in any dispersion regime. Although the spectrotemporal tunability is subject to spectral dependence, the combinatory spectral and temporal optimization through the fiber shaper enables reliable generation of high-peak-power femtosecond pulses continuously across the two-octave spectral band. To the best of our knowledge, this is the broadest continuous supercontinuum (560–2200 nm) with above-hundred kW peak power, femtosecond-level output pulses generated in silica MMFs.

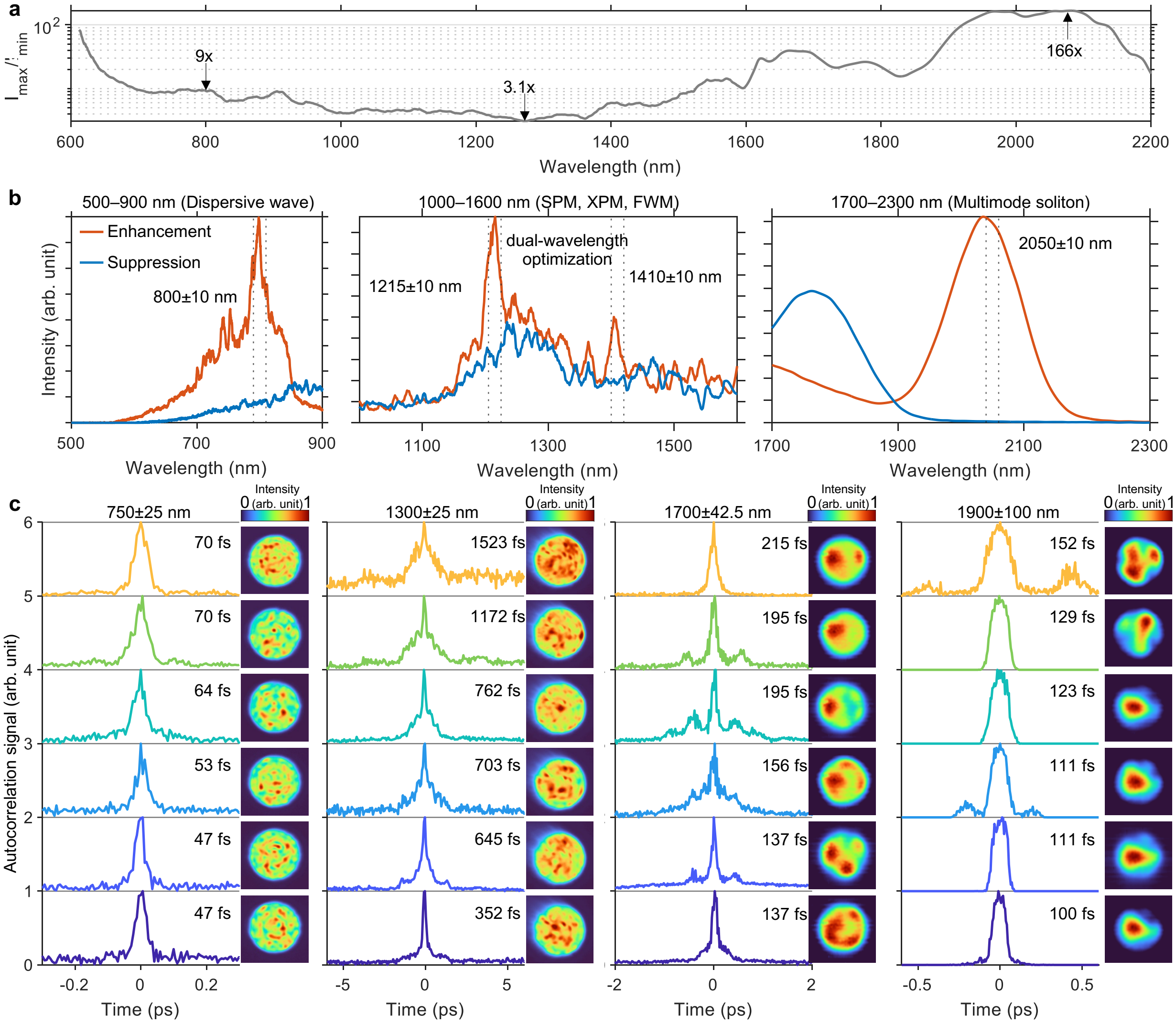

Figure 3.6: **Performance of fiber shaper: optimization in spectral, temporal, and spatial domains.** **a**, Ultrabroadband spectral tunability, evaluated from a set of spectra acquired from 3125 states of the fiber shaper. **b**,**c**, Representative examples of modulations in spectral band energy (**b**) of selected single bands and dual-band (denoted by vertical dotted lines), showing the most enhanced (Enhancement) and suppressed (Suppression) cases; and in pulse duration and the associated spatial intensity profiles (**c**) for selected spectral bands, with the center wavelength and bandwidth denoted above each panel, and the FWHM of the autocorrelation signals annotated near each trace.

Chapter 4

Enhanced Nonlinear Microscopy with Adaptive Multimode Fiber Source

4.1 Derivation of the Multiphoton Generation Efficiency

The derivation follows one of the foundational references of two-photon fluorescence (2PF) imaging [46]. The motivation of this derivation is to provide insights into how the multiphoton signal was optimized through fiber-shaper-assisted temporal and spectral shaping of the pulse.

Given the same sample, we consider how the properties of the excitation source would affect the n-photon generation efficiency, which is described by the time-averaged fluorescence photon fluxes $S_n = \langle S_n(t) \rangle$. Since we assume only the excitation source varies, we can express $S_n(t)$ solely in terms of the intensity of the excitation $I(\boldsymbol{r}, t)$, that

$$S_n(t) \propto \int_V \mathrm{d}V I^n(\boldsymbol{r}, t), \tag{4.1}$$

where V is the illuminated volume. We then express $I(\boldsymbol{r}, t)$ as $I(\boldsymbol{r}, t) = I_0(t) F(\boldsymbol{r})$ to further separate the temporal and spatial properties of the source, where $I_0(t)$ is the temporal distribution of the excitation source intensity and $F(\boldsymbol{r})$ is the normalized spatial distribution. Substitute it back to equation (4.1), we have

$$S_n \propto g^{(n)} \langle I_0(t) \rangle^n \int_V \mathrm{d}V F^n(\boldsymbol{r}), \tag{4.2}$$

where $g^{(n)} = \langle I_0^n(t) \rangle / \langle I_0(t) \rangle^n$ is the n-th order temporal coherence. In this work, the repetition rate (1 MHz) is the same for both the laser source and the MMF source, we therefore can further express the temporal term using the pulse energy E_p, pulse duration τ_p, and $g_p^{(n)}$ that only depends on the pulse shape:

$$g^{(n)} \propto \frac{g_p^{(n)}}{\tau_p^{n-1}}, \quad \langle I_0(t) \rangle \propto E_p. \tag{4.3}$$

Finally, using the normalized PSF of the source to represent $F(\boldsymbol{r})$, we arrive at

$$S_n \propto \frac{g_p^{(n)} E_p^n}{\tau_p^{n-1}} \int \mathrm{d}V \mathrm{PSF}^n(\boldsymbol{r}). \tag{4.4}$$

Equation (4.4) implies that the properties of a source that would affect the multiphoton generation efficiency are: the pulse energy E_p, the pulse duration τ_p, the PSF distribution $\mathrm{PSF}(\boldsymbol{r})$, and the factor $g_p^{(n)}$ related to the pulse shape. In the imaging section, we simplify the model by assuming different sources share the same $g_p^{(n)}$ and $\mathrm{PSF}(\boldsymbol{r})$. As a result, the fiber shaper optimization (i.e., finding the optimal actuator configuration $s \in \mathcal{S}$) can be formulated as

$$\max_{s \in \mathcal{S}} \ \frac{E_p^n(s;\lambda)}{\tau_p^{n-1}(s;\lambda)}, \tag{4.5}$$

where $\mathcal{S}$ is the space of all configurations.

Although not accounted for in the formulation, we observed that PSF can also be more confined with fiber shaper optimization. More advanced optimization scheme will be useful to further improve the spectral-temporal-spatial customization of the fiber source to push the fiber shaper to its limit.

4.2 Quantitative Analysis of the Enhancement

The results above demonstrate the potential of the fiber-shaper-controlled SI MMF for achieving a high-peak-power ultrabroadband tunable source, which is capable of modulating the output field in the spectral, temporal, and spatial domains. This capacity can facilitate diverse applications in spectroscopy, sensing, and imaging applications. As a proof-of-concept demonstration of such potential, we directly applied the proposed source for multiphoton microscopy (MPM) to investigate whether it can be adaptively optimized for nonlinear imaging which demands sources with high spectral brilliance (5–50 nJ) [47]–[49], short temporal duration (10–500 fs) [50]–[52], and confined spatial profiles [53].

We first characterized the performance of the proposed source with fluorescent beads for two-photon fluorescence (2PF) and three-photon fluorescence (3PF) imaging. For comparison, we acquired reference images with a commercial laser source based on optical parametric amplifier (OPA) from Light Conversion Cronus-3P. The results are presented in Fig. 4.1, and the experimental setup which includes the optical path for imaging and the characterization of spectral, temporal, and spatial profiles of the fiber source, is depicted in Fig. 2.1. The raw output of the MMF was directed to a scanning MPM system after passing through selected bandpass filters (750±25 nm for 2PF, 1300±25 nm and 1225±25 nm for 3PF). This setup can be readily improved in future studies with advanced wavelength selection mechanisms for more systematic and automatic multiband imaging. We observed that using the initial state of the fiber shaper, i.e., an unoptimized form, resulted in poor image quality (e.g. low multiphoton signals), which can be largely attributed to insufficient peak power due to the thinning of the energy distribution that comes with spectral broadening and/or temporal broadening caused by modal and chromatic dispersion.

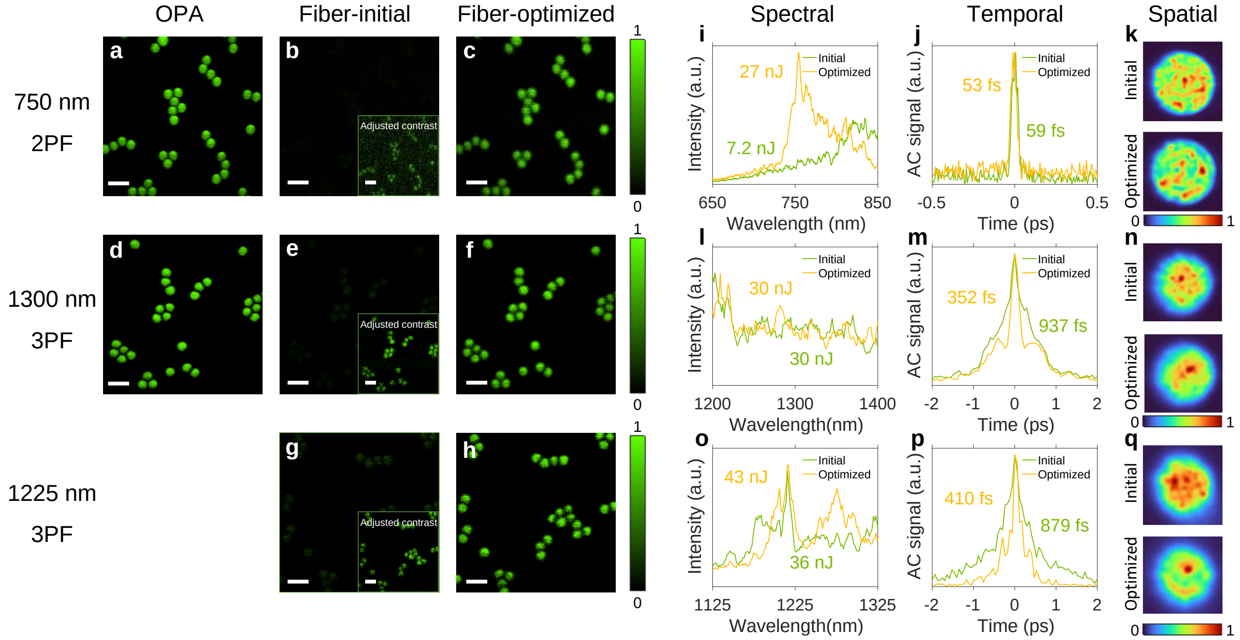

Figure 4.1: **Multiphoton microscopy with the fiber-shaper-controlled MMF source.** **a–h**, Demonstration of 2PF and 3PF imaging on fluorescent beads using OPA (**a**,**d**), initial fiber source (**b**,**e**,**g**), and optimized fiber source (**c**,**f**,**h**). The contrasts of the insets are adjusted for visibility. Scale bars: 20 µm. **i–q**, Characterization of the spectral (**i**,**l**,**o**), temporal (**j**,**m**,**p**), and spatial (**k**,**n**,**q**) properties of the output beam of the initial and optimized fiber source corresponding to the images in **a–h**. The 50-nm spectral band energy and the FWHM of the autocorrelation (AC) signals are indicated in the figures. The spatial profiles are individually normalized to their maximum intensity.

Remarkably, by adaptively and coarsely optimizing the fiber shaper using feedback from the multiphoton signals, i.e. greedy search in our experiment, enhancements of 15-fold, 11-fold and, 6-fold in signals were achieved for 2PF (750 nm), 3PF (1300 nm), and 3PF

Table 4.1: Multiphoton generation signal intensity enhancement

	E_p (nJ)	τ_p (fs)	Measured imaging signals	Calculated imaging signals
750 nm $S_2 \propto E_p^2 \tau_p$				
Initial	7.2	59	1	1
Optimized	27	53	15.10	15.65
1300 nm $S_3 \propto E_p^3 \tau_p^2$				
Initial	30	937	1	1
Optimized	30	352	10.72	7.08
1225 nm $S_3 \propto E_p^3 \tau_p^2$				
Initial	36	879	1	1
Optimized	43	410	5.82	7.83

(1225 nm) microscopy, respectively. To investigate the mechanisms of the improvement, we looked into the spectral, temporal, and spatial characteristics of the output pulses before and after optimization, and calculated the multiphoton signal generation efficiency according to the method described in [54] (Tab. 4.1). To highlight the role of spectral and temporal tuning and for simplicity, the high-order dispersions and multimodal spatial compositions are neglected in the calculation and the pulse shape and spatial profile of the fiber source are assumed to be the same as those of the laser. The strong agreement between the measured and the calculated improvements in signals confirms that pulse energy and pulse duration are the dominant factors affecting multiphoton signal generation efficiency in our experiments. Notably, the measured and calculated signal improvements for 2PF are more closely matched than those for 3PF. This can be attributed to the fact that the generation efficiency of 2PF is less dependent on the spatial distribution of the beam compared to 3PF [54].

Moreover, we observed that the output field optimization for signal enhancement of 2PF and 3PF varies as a result of different underlying mechanisms. Specifically, the signal enhancement for 2PF was primarily driven by a 3.8-fold increase in the spectral intensity at 750 nm, whereas the enhancement for 3PF signals was primarily due to a 2.7-fold (at 1300 nm) and 2.1-fold (at 1225 nm) reduction in pulse duration, resulting in peak powers of 0.72, 0.12, and 0.15 MW, assuming Gaussian pulse shape. This difference is consistent with our findings presented in Fig. 3.6, where the tunability in spectral and temporal domains exhibits strong spectral dependence due to the distinct dominant nonlinear effects: higher spectral tunability was observed in the dispersive regime (750 nm), whereas better temporal tunability was found in the nonlinear phase modulation regime (1300 and 1225 nm). Additionally, we observed that the corresponding spatial profile of 3PF showed a tendency to be less speckled and more confined when the pulse was shortened, due to a reduced modal dispersion. The reduction in speckling in 3PF is likely to result in less image blurring compared to 2PF.

4.3 Point Spread Function Engineering

To provide insights into the imaging quality of the 3PF compared to the 2PF, we first used 0.1-µm beads (Bangs Laboratories FCDG002) to measure the PSFs for both 2PF and 3PF excitation with the multimode fiber (MMF) source, together with 3PF excitation with the laser (Cronus-3P) as the gold standard reference. As shown in Fig. 4.2, the 3PF excitation PSF using the laser had a full width at half maximum (FWHM) of approximately 0.57 µm. For the fiber source, the FWHM for the 2PF excitation was 1.52 µm and for 3PF was 0.85 µm. The smaller PSF for the 3PF excitation can explain why less image blurring occurred compared to 2PF excitation.

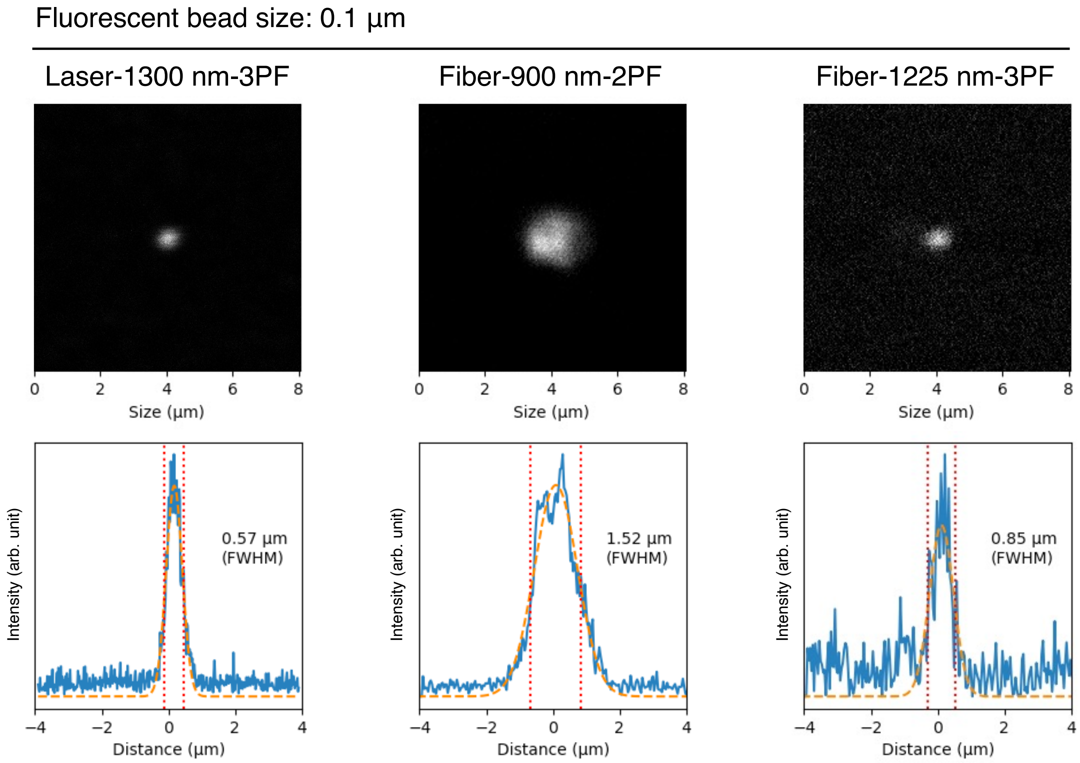

Figure 4.2: **PSF measurement of the 3PF excitation with the laser (reference) and the 2PF and 3PF excitation with the fiber source.** The size of the bead is 0.1 µm.

To further illustrate how fiber shaper configurations directly affect the imaging PSF, we have provided experimental data of the changing PSFs in relation to different fiber shaper configurations, as suggested by the reviewer. We started the experiment with 0.1-µm beads

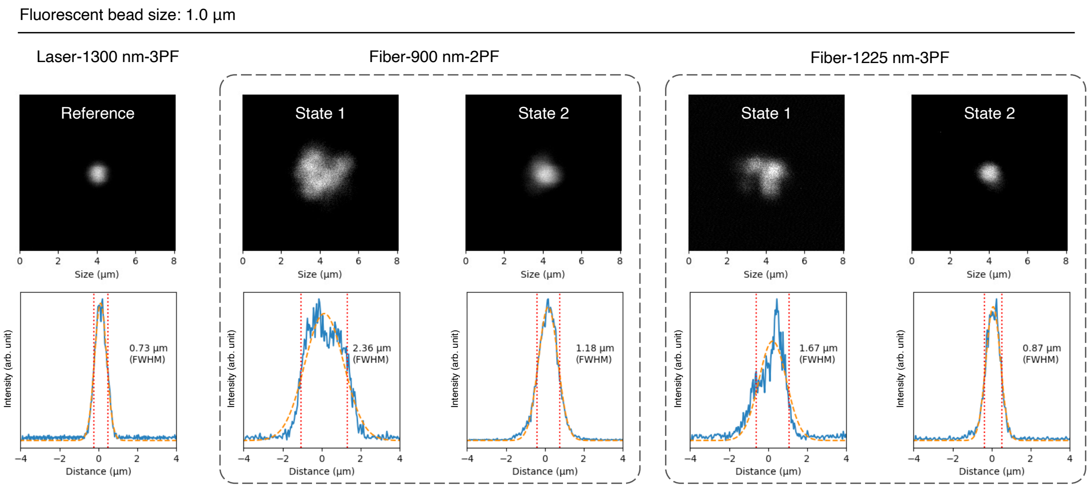

Figure 4.3: **Qualitative PSF comparison of the 2PF excitation (900 nm) and the 3PF excitation (1300 nm) with the fiber source under random bending conditions induced by the fiber shaper's different states.**The size of the bead is 1 µm.

as shown in Fig. 4.2. However, we observed significant signal attenuation during the continuous scanning of the 0.1-µm beads, likely due to photobleaching, which makes it technically challenging to continuously and reliably monitor the PSF variations during different bending conditions. This issue can be addressed by purchasing brighter beads. For illustration purposes, we monitored how different bending configurations modify the PSFs using 1.0-µm beads (Bangs Laboratories FCDG006) to ensure a higher and more stable level of signals, as shown in Fig. 4.3. While some configurations (e.g., an optimized fiber shaper configuration state 2 in 900-nm for 2PF and 1225-nm for 3PF) showed near-Gaussian PSFs, certain configurations (e.g., the initial fiber shaper configuration state 1) showed significantly different PSFs. In particular, 3PF can be more sensitive to the changes in the fiber output spatial profiles than 2PF because of its higher nonlinearity. Therefore, the changes in the PSFs shown in Fig. 4.3, as a result of the modulated fiber output, are very likely responsible for the 34% discrepancy between the predicted and experimental values of signal improvement in 3PF. We would like to note that, while we only optimized the spectral band energy for the proof-of-concept experiment, optimizing PSFs together with the spectral properties is very promising in the future work since the proposed fiber shaper has demonstrated the capability of spatial control, as shown in Fig. 4.4.

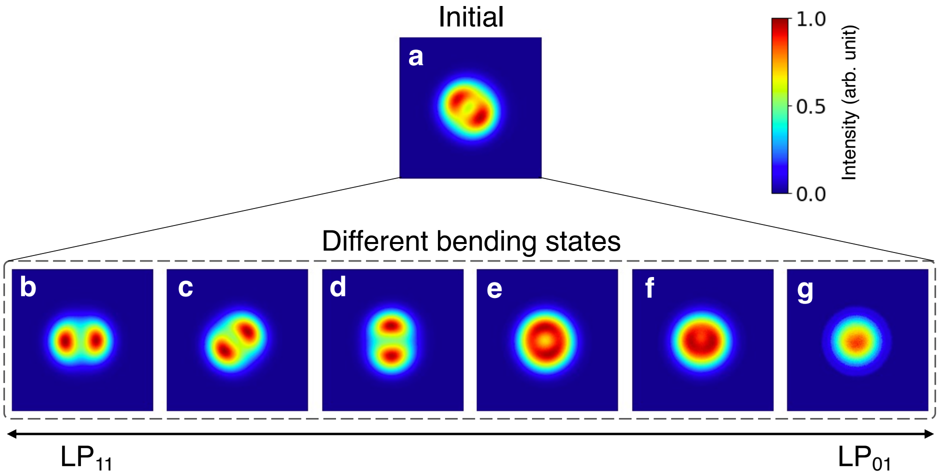

Figure 4.4: **Normalized output spatial profiles of a 10-µm core step-index multimode fiber under various bending conditions.** **a**, Initial near-field intensity profile of the fiber output, showing a mixture of approximately three spatial linearly polarized (LP) modes. **b-g**, Near-field intensity profiles of the fiber output under various bending conditions, showing different combinations of the LP_{01} and the LP_{11} with two-fold spatial degeneracy. Each profile is individually normalized.

4.4 Label-free Nonlinear Microscopy on Tissues

The multiphoton microscopy images were acquired using a custom-built inverted scanning microscope. The microscope used a pair of galvanometer mirrors (ScannerMAX Saturn-5 Galvo and Saturn-9 Galvo) to scan the beam. The beam was then focused by a water immersion objective (Olympus XLPLN25XWMP2, 1.05 NA). The emitted photons were collected using a photomultiplier (Thorlabs PMT2101). During imaging, the fiber source was pumped by 800 nJ 46 fs pulses at 1300 nm and 1 MHz repetition rate.

Fluorescent carboxyl polystyrene (Bangs Laboratories Inc FCDG009) was used as the imaging sample for characterization, a proper emission filter (Edmund Optics 530±22.5 nm) was chosen to match its fluorescence emission spectrum. Tissue from whisker pad was used in label-free imaging, where emission filters (Semrock 609±28.5 nm, Edmund Optics 530±22.5 nm, Thorlabs 405±5 nm) were chosen for collecting the SHG, 3PAF, and THG signals, respectively. The tissue sample images were acquired with a 30-µs pixel dwelling time and a 900-µm field of view, and 4×4 images were stitched to represent the mosaicked image. The greedy search method was implemented with the imaging signals as feedback. Specifically, the displacement of each actuator on the fiber shaper was sequentially chosen with the imaging signals maximized.

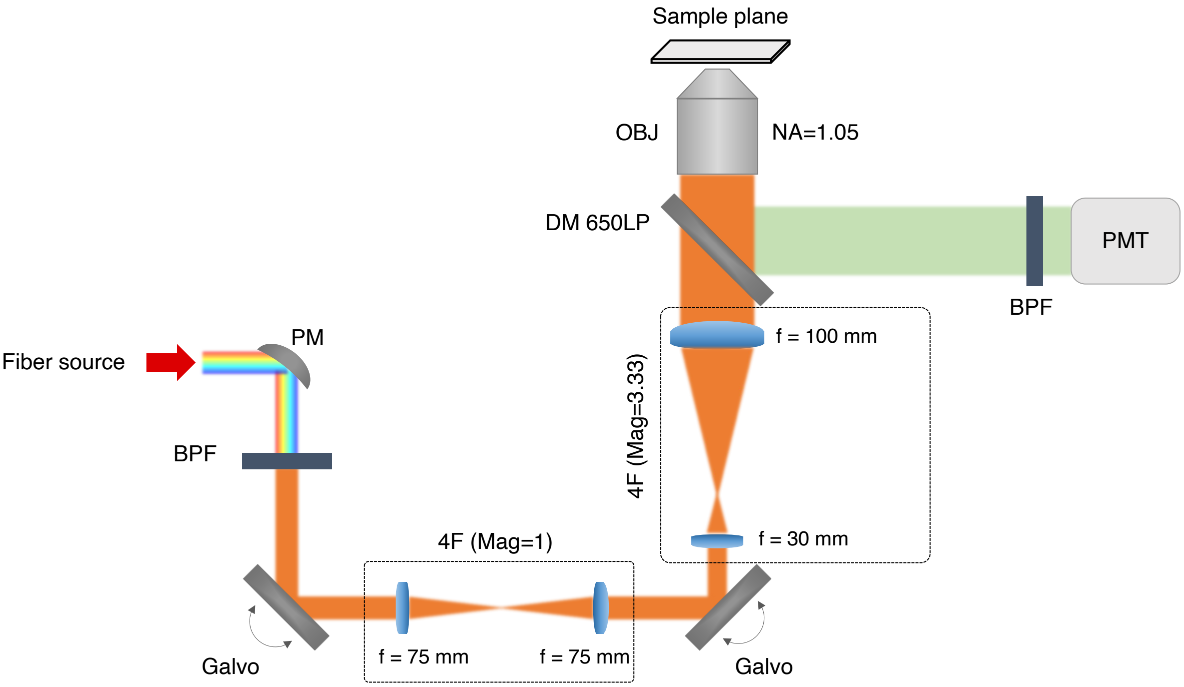
Sample plane
OBJ
NA=1.05
DM 650LP
PMT
BPF
f = 100 mm
4F (Mag=3.33)
Fiber source
PM
BPF
f = 30 mm
4F (Mag=1)
Galvo
f = 75 mm
f = 75 mm
Galvo

Figure 4.5: **Schematic of the multiphoton imaging setup.** PM: parabolic mirror; BPF: bandpass filter; DM: dichroic mirror; LP: long pass; OBJ: objective lens; PMT: photomultiplier tube.

We next examined the performance of the proposed source for label-free imaging of freshly excised mouse tissue. The multiphoton imaging setup is shown in Fig. 4.5. We selected the 1225±25 nm excitation band, which is not covered by most commercial high-power OPA or low-rep high-peak-power lasers. After the same procedure of optimization (greedy search based on the imaging signals), the optimized SI MMF allows the simultaneous visualization of adipocytes through third-harmonic generation (THG), muscles through three-photon autofluorescence (3PAF), and collagen fibers through second-harmonic generation (SHG) (Fig. 4.6), which demonstrated the potential of this source as a widely and continuously tunable source for biomedical imaging.

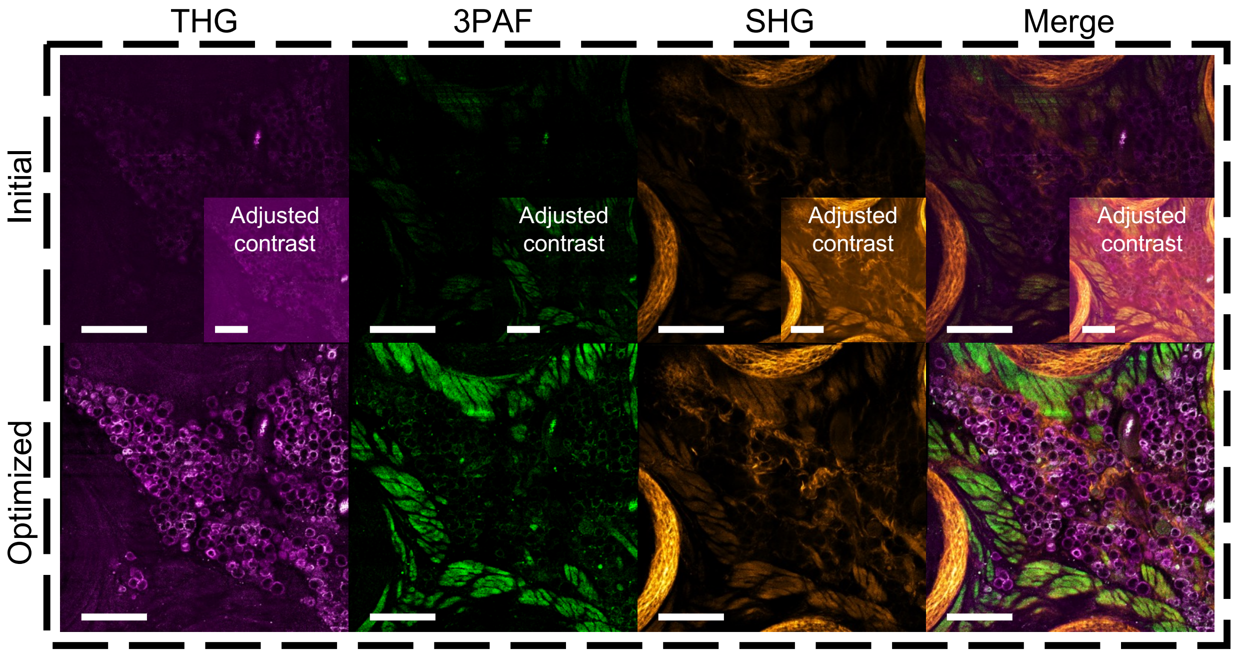
THG
3PAF
SHG
Merge
Initial
Optimized
Adjusted contrast
Adjusted contrast
Adjusted contrast
Adjusted contrast

Figure 4.6: **Nonlinear Microscopy with Adaptive Fiber source** Mouse whisker pad tissue imaging at 1225 nm excitation using the initial and optimized fiber source, showing THG signals of adipocytes, 3PAF signals of muscles, and SHG signals of collagen fibers. The contrasts of the insets are adjusted for visibility. Scale bars: 200 µm.

Chapter 5

Conclusion

In summary, we have presented a new way of controlling nonlinear effects by leveraging both the spatial and temporal degrees of freedom through a programmable fiber shaper. This method unlocks access to an even higher-dimensional space of spatiotemporal dynamics and two-octave-wide high peak power in an off-the-shelf SI MMF. The major contributions of this work include (1) opening up novel perspectives for spatiotemporal control of nonlinear multimode pulse propagation, (2) proposing an avenue for power scaling and field control of broadband sources from visible to NIR-IR regime, and (3) providing accessible and open-source control designs that can be rapidly adopted for both nonlinear and linear modulation of multimode fibers.

Compared to other methods for spatiotemporal light control, our proposed method directly modulates the modal interactions during the pulse temporal evolution using a slip-on 3D-printed fiber shaper, without additional non-fiber modulation layers such as free-space spatial light modulators for wavefront shaping in spatial and temporal domains. The all-fiber route to single-stage nonlinear conversion inherently contributes to stronger alignment robustness, greater long-term stability, and higher spectral band energy. Compared to the commonly used GRIN MMFs, the higher damage threshold and the significantly higher tunability of SI MMFs make it an essential part of the unprecedented spatiotemporal control of the high-power multimodal nonlinear effects. As a result, the proposed apparatus leads to a fiber source with high broadband spectral brilliance averaging at 0.415 nJ/nm across a wide bandwidth from 560 to 2200 nm, femtosecond-level output pulse duration, and great spectrotemporal tunability. We demonstrated an average of 25-fold (up to 166-fold) enhancement in spectral band energy, and up to 4.3-fold reduction in pulse duration.

The fiber shaper enabled combined spectral and temporal tuning, leading to high peak power levels across two-octave spectral bands. For instance, at 750±25 nm, the peak power reached 0.72 MW and 0.15 MW at 1225±25 nm, surpassing the expected regime of operation, which is usually the soliton regime for its inherently high spectral density and short pulse duration. These performances (1) overcome the bandwidth limitation of existing high-peak-power fiber sources based on soliton formation and (2) demonstrate orders of magnitude higher peak power compared to existing tunable fiber-based broadband sources. These properties could benefit the emerging but technologically demanding applications in optical sensing, imaging, manipulation, and computing, that require light sources with broad spectral coverage, great tunability, ultrafast pulses (femtosecond-level pulse duration), stability, and/or high spectral density of energy and peak power.

Future research could investigate the scalability of the proposed approach to larger core-size MMFs and higher peak powers, enabling the development of compact and high-power tunable light sources for industrial and scientific applications

References

[1] F. Poletti and P. Horak, “Description of ultrashort pulse propagation in multimode optical fibers,” *JOSA B*, vol. 25, no. 10, pp. 1645–1654, 2008.

[2] W. H. Renninger and F. W. Wise, “Optical solitons in graded-index multimode fibres,” *Nature communications*, vol. 4, no. 1, p. 1719, 2013.

[3] A. S. Ahsan and G. P. Agrawal, “Graded-index solitons in multimode fibers,” *Optics Letters*, vol. 43, no. 14, pp. 3345–3348, 2018.

[4] L. Rishøj, B. Tai, P. Kristensen, and S. Ramachandran, “Soliton self-mode conversion: Revisiting raman scattering of ultrashort pulses,” *Optica*, vol. 6, no. 3, pp. 304–308, 2019.

[5] G. P. Agrawal, “Invite paper: Self-imaging in multimode graded-index fibers and its impact on the nonlinear phenomena,” *Optical Fiber Technology*, vol. 50, pp. 309–316, 2019.

[6] M. Eftekhar, Z. Sanjabi-Eznaveh, H. Lopez-Aviles, S. Benis, J. Antonio-Lopez, M. Kolesik, F. Wise, R. Amezcua-Correa, and D. Christodoulides, “Accelerated nonlinear interactions in graded-index multimode fibers,” *Nature communications*, vol. 10, no. 1, p. 1638, 2019.

[7] L. G. Wright, W. H. Renninger, D. N. Christodoulides, and F. W. Wise, “Nonlinear multimode photonics: Nonlinear optics with many degrees of freedom,” *Optica*, vol. 9, no. 7, pp. 824–841, 2022.

[8] E. V. Podivilov, D. S. Kharenko, V. Gonta, K. Krupa, O. S. Sidelnikov, S. Turitsyn, M. P. Fedoruk, S. A. Babin, and S. Wabnitz, “Hydrodynamic 2d turbulence and spatial beam condensation in multimode optical fibers,” *Physical review letters*, vol. 122, no. 10, p. 103 902, 2019.

[9] R. M. Koehl, T. Hattori, and K. A. Nelson, “Automated spatial and temporal shaping of femtosecond pulses,” *Optics communications*, vol. 157, no. 1-6, pp. 57–61, 1998.

[10] J. C. Vaughan, T. Feurer, and K. A. Nelson, "Automated two-dimensional femtosecond pulse shaping," *JOSA B*, vol. 19, no. 10, pp. 2489–2495, 2002.

[11] J. Wang and Y. Liang, "Generation and detection of structured light: A review," *Frontiers in Physics*, vol. 9, p. 688 284, 2021.

[12] A. Picozzi, J. Garnier, T. Hansson, P. Suret, S. Randoux, G. Millot, and D. N. Christodoulides, "Optical wave turbulence: Towards a unified nonequilibrium thermodynamic formulation of statistical nonlinear optics," *Physics Reports*, vol. 542, no. 1, pp. 1–132, 2014.

[13] J. Garnier, A. Fusaro, K. Baudin, C. Michel, K. Krupa, G. Millot, and A. Picozzi, "Wave condensation with weak disorder versus beam self-cleaning in multimode fibers," *Physical Review A*, vol. 100, no. 5, p. 053 835, 2019.

[14] A. Mussot, T. Sylvestre, L. Provino, and H. Maillotte, "Generation of a broadband single-mode supercontinuum in a conventional dispersion-shifted fiber by use of a subnanosecond microchiplaser," *Optics Letters*, vol. 28, no. 19, pp. 1820–1822, 2003.

[15] J. Cheng, M. E. Pedersen, K. Charan, K. Wang, C. Xu, L. Grüner-Nielsen, and D. Jakobsen, "Intermodal čerenkov radiation in a higher-order-mode fiber," *Optics Letters*, vol. 37, no. 21, pp. 4410–4412, 2012.

[16] J. Demas, P. Steinvurzel, B. Tai, L. Rishoj, Y. Chen, and S. Ramachandran, "Intermodal nonlinear mixing with bessel beams in optical fiber," *Optica*, vol. 2, no. 1, pp. 14–17, 2015.

[17] E. Nazemosadat, H. Pourbeyram, and A. Mafi, "Phase matching for spontaneous frequency conversion via four-wave mixing in graded-index multimode optical fibers," *JOSA B*, vol. 33, no. 2, pp. 144–150, 2016.

[18] L. G. Wright, D. N. Christodoulides, and F. W. Wise, "Controllable spatiotemporal nonlinear effects in multimode fibres," *Nature photonics*, vol. 9, no. 5, pp. 306–310, 2015.

[19] M. A. Eftekhar, L. Wright, M. Mills, M. Kolesik, R. A. Correa, F. W. Wise, and D. N. Christodoulides, "Versatile supercontinuum generation in parabolic multimode optical fibers," *Optics Express*, vol. 25, no. 8, pp. 9078–9087, 2017.

[20] O. Tzang, A. M. Caravaca-Aguirre, K. Wagner, and R. Piestun, "Adaptive wavefront shaping for controlling nonlinear multimode interactions in optical fibres," *Nature Photonics*, vol. 12, no. 6, pp. 368–374, 2018.

[21] E. Deliancourt, M. Fabert, A. Tonello, K. Krupa, A. Desfarges-Berthelemot, V. Kermene, G. Millot, A. Barthélémy, S. Wabnitz, and V. Couderc, "Wavefront shaping for optimized many-mode kerr beam self-cleaning in graded-index multimode fiber," *Optics Express*, vol. 27, no. 12, pp. 17 311–17 321, 2019.

[22] U. Teğin, B. Rahmani, E. Kakkava, N. Borhani, C. Moser, and D. Psaltis, "Controlling spatiotemporal nonlinearities in multimode fibers with deep neural networks," *Apl Photonics*, vol. 5, no. 3, p. 030 804, 2020.

[23] X. Wei, J. C. Jing, Y. Shen, and L. V. Wang, "Harnessing a multi-dimensional fibre laser using genetic wavefront shaping," *Light: Science & Applications*, vol. 9, no. 1, p. 149, 2020.

[24] S. Resisi, Y. Viernik, S. M. Popoff, and Y. Bromberg, "Wavefront shaping in multimode fibers by transmission matrix engineering," *APL Photonics*, vol. 5, no. 3, p. 036 103, 2020.

[25] D. V. Regelman, Y. Segev, and S. Yosub, *Method for brightness enhancement and modes manipulation of a multimode optical fiber*, US Patent 9,329,416, May 2016.

[26] D. Golubchik, Y. Segev, and D. Regelman, "Controlled mode mixing in optical fibers," in *International Conference and Exhibition on Optics and Electro-Optics (OASIS 5)*, 2015.

[27] Z. Finkelstein, K. Sulimany, S. Resisi, and Y. Bromberg, "Spectral shaping in a multimode fiber by all-fiber modulation," *APL Photonics*, vol. 8, no. 3, p. 036 110, 2023.

[28] A. W. Snyder, "Coupled-mode theory for optical fibers," *JOSA*, vol. 62, no. 11, pp. 1267–1277, 1972.

[29] D. Marcuse, "Coupled mode theory of round optical fibers," *Bell System Technical Journal*, vol. 52, no. 6, pp. 817–842, 1973.

[30] L. G. Wright, W. H. Renninger, D. N. Christodoulides, and F. W. Wise, "Spatiotemporal dynamics of multimode optical solitons," *Optics Express*, vol. 23, no. 3, pp. 3492–3506, 2015.

[31] M. Eftekhar, H. Lopez-Aviles, F. Wise, R. Amezcua-Correa, and D. Christodoulides, "General theory and observation of cherenkov radiation induced by multimode solitons," *Communications Physics*, vol. 4, no. 1, p. 137, 2021.

[32] M. Zitelli, Y. Sun, M. Ferraro, F. Mangini, O. Sidelnikov, V. Couderc, and S. Wabnitz, "Multimode solitons in step-index fibers," *Optics Express*, vol. 30, no. 4, pp. 6300–6310, 2022.

[33] A. Dubietis, G. Tamošauskas, R. Šuminas, V. Jukna, and A. Couairon, "Ultrafast supercontinuum generation in bulk condensed media (invited review)," *arXiv preprint arXiv:1706.04356*, 2017.

[34] A. L. Gaeta, "Catastrophic collapse of ultrashort pulses," *Physical Review Letters*, vol. 84, no. 16, p. 3582, 2000.

[35] P. Horak and F. Poletti, "Multimode nonlinear fibre optics: Theory and applications," *Recent progress in optical fiber research*, vol. 3, 2012.

[36] L. G. Wright, Z. M. Ziegler, P. M. Lushnikov, Z. Zhu, M. A. Eftekhar, D. N. Christodoulides, and F. W. Wise, "Multimode nonlinear fiber optics: Massively parallel numerical solver, tutorial, and outlook," *IEEE Journal of Selected Topics in Quantum Electronics*, vol. 24, no. 3, pp. 1–16, 2017.

[37] Y. Xiao, R.-J. Essiambre, M. Desgroseilliers, A. M. Tulino, R. Ryf, S. Mumtaz, and G. P. Agrawal, "Theory of intermodal four-wave mixing with random linear mode coupling in few-mode fibers," *Optics Express*, vol. 22, no. 26, pp. 32 039–32 059, 2014.

[38] A. Bendahmane, K. Krupa, A. Tonello, D. Modotto, T. Sylvestre, V. Couderc, S. Wabnitz, and G. Millot, "Seeded intermodal four-wave mixing in a highly multimode fiber," *JOSA B*, vol. 35, no. 2, pp. 295–301, 2018.

[39] S. Mumtaz, R.-J. Essiambre, and G. P. Agrawal, "Nonlinear propagation in multimode and multicore fibers: Generalization of the manakov equations," *Journal of Lightwave Technology*, vol. 31, no. 3, pp. 398–406, 2012.

[40] A. Yariv, "Coupled-mode theory for guided-wave optics," *IEEE Journal of Quantum Electronics*, vol. 9, no. 9, pp. 919–933, 1973.

[41] R. Olshansky, "Mode coupling effects in graded-index optical fibers," *Applied optics*, vol. 14, no. 4, pp. 935–945, 1975.

[42] A. M. Caravaca-Aguirre and R. Piestun, "Single multimode fiber endoscope," *Optics Express*, vol. 25, no. 3, pp. 1656–1665, 2017.

[43] D. E. B. Flaes, J. Stopka, S. Turtaev, J. F. De Boer, T. Tyc, and T. Čižmár, "Robustness of light-transport processes to bending deformations in graded-index multimode waveguides," *Physical review letters*, vol. 120, no. 23, p. 233 901, 2018.

[44] J. Carpenter, B. C. Thomsen, and T. D. Wilkinson, "Degenerate mode-group division multiplexing," *Journal of Lightwave Technology*, vol. 30, no. 24, pp. 3946–3952, 2012.

[45] M. Lancry, B. Poumellec, A. Chahid-Erraji, M. Beresna, and P. Kazansky, “Dependence of the femtosecond laser refractive index change thresholds on the chemical composition of doped-silica glasses,” *Optical Materials Express*, vol. 1, no. 4, pp. 711–723, 2011.

[46] C. Xu and W. W. Webb, “Measurement of two-photon excitation cross sections of molecular fluorophores with data from 690 to 1050 nm,” *JOSA B*, vol. 13, no. 3, pp. 481–491, 1996.

[47] M. Yildirim, H. Sugihara, P. T. So, and M. Sur, “Functional imaging of visual cortical layers and subplate in awake mice with optimized three-photon microscopy,” *Nature communications*, vol. 10, no. 1, p. 177, 2019.

[48] S. You, H. Tu, E. J. Chaney, Y. Sun, Y. Zhao, A. J. Bower, Y.-Z. Liu, M. Marjanovic, S. Sinha, Y. Pu, *et al.*, “Intravital imaging by simultaneous label-free autofluorescence-multiharmonic microscopy,” *Nature communications*, vol. 9, no. 1, p. 2125, 2018.

[49] K. Choe, Y. Hontani, T. Wang, E. Hebert, D. G. Ouzounov, K. Lai, A. Singh, W. Béguelin, A. M. Melnick, and C. Xu, “Intravital three-photon microscopy allows visualization over the entire depth of mouse lymph nodes,” *Nature Immunology*, vol. 23, no. 2, pp. 330–340, 2022.

[50] E. E. Hoover and J. A. Squier, “Advances in multiphoton microscopy technology,” *Nature photonics*, vol. 7, no. 2, pp. 93–101, 2013.

[51] D. Debarre, N. Olivier, W. Supatto, and E. Beaurepaire, “Mitigating phototoxicity during multiphoton microscopy of live drosophila embryos in the 1.0–1.2 μ m wavelength range,” *PLoS One*, vol. 9, no. 8, e104250, 2014.

[52] D. M. Huland, K. Charan, D. G. Ouzounov, J. S. Jones, N. Nishimura, and C. Xu, “Three-photon excited fluorescence imaging of unstained tissue using a grin lens endoscope,” *Biomedical Optics Express*, vol. 4, no. 5, pp. 652–658, 2013.

[53] C.-Y. Dong, K. Koenig, and P. So, “Characterizing point spread functions of two-photon fluorescence microscopy in turbid medium,” *Journal of biomedical optics*, vol. 8, no. 3, pp. 450–459, 2003.

[54] C. Xu and W. W. Webb, “Multiphoton excitation of molecular fluorophores and nonlinear laser microscopy,” *Topics in Fluorescence Spectroscopy: Volume 5: Nonlinear and Two-Photon-Induced Fluorescence*, pp. 471–540, 2002.